Int J Comput Vis (2008) 78: 89–105
DOI 10.1007/s11263-007-0082-8

Identical Projective Geometric Properties of Central Catadioptric Line Images and Sphere Images with Applications to Calibration

Xianghua Ying · Hongbin Zha

Received: 26 November 2006 / Accepted: 14 August 2007 / Published online: 3 October 2007

Abstract Central catadioptric cameras are imaging devices that use mirrors to enhance the field of view while preserving a single effective viewpoint. Lines and spheres in space are all projected into conics in the central catadioptric image planes, and such conics are called line images and sphere images, respectively. We discovered that there exists an imaginary conic in the central catadioptric image planes, defined as the modified image of the absolute conic (MIAC), and by utilizing the MIAC, the novel identical projective geometric properties of line images and sphere images may be exploited: Each line image or each sphere image is double-contact with the MIAC, which is an analogy of the discovery in pinhole camera that the image of the absolute conic (IAC) is double-contact with sphere images. Note that the IAC also exists in the central catadioptric image plane, but it does not have the double-contact properties with line images or sphere images. This is the main reason to propose the MIAC. From these geometric properties with the MIAC, two linear calibration methods for central catadioptric cameras using sphere images as well as using line images are proposed in the same framework. Note that there are many linear approaches to central catadioptric camera calibration using line images. It seems that to use the properties that line images are tangent to the MIAC only leads to an alternative geometric construction for calibration. However, for sphere images, there are only some nonlinear calibration methods in literature. Therefore, to propose linear methods for sphere images may be the main contribution of this paper. Our new algorithms have been tested in extensive experiments with respect to noise sensitivity.

Keywords Catadioptric camera, · Omnidirectional vision · Camera calibration · Line image · Sphere image · Double-contact theorem

1 Introduction

Catadioptric cameras are imaging systems consisting of refracting lenses (dioptrics) and reflecting mirrors (catoptrics) as defined by Hecht and Zajac (1997). Some representative implementations of catadioptric imaging systems are described in Nayar (1988); Yagi and Kawato (1990); Hong et al. (1991); Bogner (1995); Nalwa (1996); Svoboda et al. (1998); Yagi and Yachida (2004); Swaminathan et al. (2006). Catadioptric systems with respect to a single effective viewpoint are thoroughly investigated by Baker and Nayar (1998), and which satisfy the single viewpoint constraint are called central catadioptric cameras. The reason to desire a single viewpoint is that it can generate geometrically correct perspective images from the images captured by the central catadioptric cameras. Since existing vision algorithms primarily utilize the single viewpoint model, i.e., the well-known pinhole camera model, it is not difficult to extend these algorithms directly for calibrated central catadioptric cameras.

This paper addresses calibration issues in central catadioptric cameras. Previous approaches may be classified into three categories: using control points with known world coordinates (Aliaga 2001), self-calibration (Kang 2000), and using line images or sphere images (Geyer and Daniilidis 1999, 2002; Barreto and Araujo 2001; Ying and Hu 2004;

X. Ying (✉) · H. Zha
National Laboratory on Machine Perception, Peking University, Beijing 100871, China
e-mail: xhying@cis.pku.edu.cn

H. Zha
e-mail: zha@cis.pku.edu.cn

Barreto and Araujo 2005). The motivation of this paper is to find linear calibration methods for central catadioptric cameras using sphere images as well as line images in the same framework. We draw inspiration from the study on the pinhole camera calibration using sphere images (Agrawal and Davis 2003; Teramoto and Xu 2002; Ying and Zha 2005, 2006), which will be introduced later.

1.1 Related Work on Central Catadioptric Camera Calibration Using Line Images or Sphere Images

This kind of methods only uses the images of lines or spheres in the scene, without knowledge of any metric information. Geyer and Daniilidis (1999) used images of two sets of parallel lines to find the intrinsic parameters as well as the orientation of the plane containing the two parallel line sets. Barreto and Araujo (2001) presented a two-step method: Firstly, the principal point is determined using the intersections of three catadioptric line images. Secondly, the recovered principal point is used to determine the image of the absolute conic from these line images, and finally the intrinsic parameters are recovered by means of Cholesky factorization. Geyer and Daniilidis (2002) proposed another calibration method for a catadioptric camera with a parabolic mirror using the projective properties of the images of three lines. Barreto and Araujo (2005) proposed a geometric construction method using the geometric properties of line images for any central catadioptric camera which is generalized previous results for paracatadioptric cameras. They proved that three line images are enough to compute the mirror and the intrinsic parameters. They also showed that the hyperbolic system can be calibrated using only two line images. Recently, Ying and Hu (2004) proved that a line image can provide three invariants whereas a sphere image can only provide two. From these invariants, constraint equations for the intrinsic parameters of catadioptric camera are derived. In general, two line images or three sphere images are sufficient to achieve catadioptric camera calibration. One important observation in Ying and Hu (2004) is that the method based on sphere images is more robust and has higher accuracy than that based on line images. The main underlying reason is that, the projection of a line (usually a line segment in real scene) is only a small arc of a conic (e.g. about one-third of an ellipse) but the projection of a sphere is usually a closed ellipse, and conic fitting using points lying on a portion of a conic is an error-prone process. However, the calibration methods proposed by Ying and Hu (2004) employ nonlinear optimization method and requires a good initial estimation to start the minimization. Most recently, Barreto and Araujo (2006) proposed a very efficient conic fitting method for line images under paracatadioptric cameras to obtain more accurate estimations. However, for the hyperbolic case, the problem of line image fitting is still open.

1.2 Related Work on Pinhole Camera Calibration Using Sphere Images

The image of the absolute conic (IAC) plays a central role in camera calibration. Teramoto and Xu (2002) first discovered the algebraic relation between the sphere image and the IAC under a pinhole camera, and then provided an efficient algorithm to solve for the camera parameters. However, in their approach the minimization is accomplished by means of a general-purpose nonlinear minimization and required a good initial estimation to start the minimization. Agrawal and Davis (2003) utilized the dual representation instead, i.e., the algebraic relation between the dual form of a sphere image and the dual image of the absolute conic (DIAC), then employed semi-definite programming (SDP) to solve for the intrinsic parameters without requiring initial estimations. Base on the main principles derived in Teramoto and Xu (2002) and Agrawal and Davis (2003), we (Ying and Zha 2005, 2006) further discovered that each sphere image is tangent to the IAC at two double-contact image points, and some linear calibration methods are derived from this observation. Zhang et al. (2007) introduced a novel approach for solving the problem of camera calibration from spheres by exploiting the relationship between the dual images of spheres and the dual image of the absolute conic, it is shown that the common pole and polar with regard to the conic images of two spheres are also the pole and polar with regard to the IAC. This provides two constraints for estimating the IAC and, hence, allows a camera to be calibrated from an image of at least three spheres.

1.3 Contributions of This Paper

Based on the discovery in pinhole that a sphere image is double contact with the IAC (Ying and Zha 2005, 2006), we further reveal that there also exists a conic with purely imaginary points in the central catadioptric image planes analogy to the IAC in pinhole, called the modified image of the absolute conic (MIAC, its definition is described in the main text), which is double contact with each line image or each sphere image under central catadioptric cameras. Note that the IAC also exists in the central catadioptric image plane, but the IAC is no longer double-contact with line images or sphere images under central catadioptric cameras. It has four intersections (real and imaginary) in general with each line image or each sphere image. This is the main reason to propose the MIAC for central catadioptric cameras. Furthermore, the methods for pinhole camera calibration using sphere images proposed in Ying and Zha (2005, 2006) are extended to central catadioptric camera calibration using line images or sphere images. Note that the central catadioptric camera with planar mirror is equivalent to a pinhole camera, i.e., the pinhole camera may be treated as a special

case of central catadioptric cameras. Therefore, this paper may be considered as an intuitive extension from pinhole to central catadioptric. However, in fact, to prove the feasibility of this extension is not easy as demonstrated in the main text.

The main contributions of this paper are emphasized as follows:

1. The MIAC is firstly discovered and introduced for central catadioptric camera calibration by us, which is an analogy of the IAC for pinhole camera in some respects. In-depth analyses of the relation between the MIAC and the IAC are presented.
2. Some novel geometric properties are discovered that each line image and each sphere image is double-contact with the MIAC. Note that to find these properties is not trivial. It is not only an intuitive guess but also requires rigorous proofs.
3. The double-contact theorem is employed to interpret the relations among the MIAC and line images or sphere images. In addition, a new geometric approach is proposed to determine the chord of contact between the MIAC and a line image or a sphere image, which is a very important part and only algebraic approach is given in previous calibration algorithms (Agrawal and Davis 2003; Ying and Zha 2005, 2006).
4. Two new linear calibration methods are proposed while dealing with line images and sphere images in a unified framework. Note that there are many linear approaches to central catadioptric camera calibration using line images. It seems that to use the properties that line images are tangent to the MIAC only leads to an alternative geometric construction for calibration. However, for sphere images, there are only some nonlinear calibration methods in literature.

This paper is organized as follows: Sect. 2 briefly introduces some notations and basic principles. The novel identical projective geometric properties of line images and sphere images are proposed in Sect. 3 and Sect. 4. Two new calibration algorithms are derived from these properties as shown in Sect. 5. Experimental results are demonstrated in Sect. 6. Finally, Sect. 7 presents some concluding remarks.

2 Imaging Models and Equations of Central Catadioptric Line Images and Sphere Images

2.1 Pinhole Camera Model

Given a 3D point $\mathbf{M} = [X\ Y\ Z\ 1]^T$ and its image $\mathbf{m} = [u\ v\ 1]^T$, both in the homogeneous coordinates, the relationship between 3D world coordinates and 2D image coordinates may be written in matrix form as,

$$\mu\mathbf{m} = \mathbf{PM}, \tag{1}$$

where $\mathbf{P}$ is a 3×4 projection matrix describing the perspective projection process. μ is an unknown scale factor. The projection matrix may be decomposed as:

$$\mathbf{P} = \mathbf{K}[\mathbf{R}|\mathbf{t}], \tag{2}$$

where

$$\mathbf{K} = \begin{bmatrix} f_x & s & u_0 \\ 0 & f_y & v_0 \\ 0 & 0 & 1 \end{bmatrix}. \tag{3}$$

Here the upper triangular matrix $\mathbf{K}$ is the matrix of the intrinsic parameters, and $(\mathbf{R}, \mathbf{t})$ denote a rigid transformation which indicate the orientation and position of the camera with respect to the world coordinate system.

2.2 A Generalized Image Formation Model for Central Catadioptric Cameras

Geyer and Daniilidis (2001) proposed a generalized image formation model for central catadioptric cameras, and proved that the central catadioptric image formation is equivalent to a two-step mapping via a sphere (see Fig. 1):

Step 1: A point in 3D space is projected to a point on a unit sphere centered at the single effective viewpoint O. The unit sphere is called the viewing sphere.

Step 2: The point on the viewing sphere is perspectively projected to a point on the image plane Π from another point O_C. The image plane Π is perpendicular to the line determined by the single viewpoint O and O_C.

This step can be considered as taking image of the viewing sphere using a virtual camera whose optical center is located in O_C and whose optical axis coincides with the line determined by O and O_C. We denote the distance $l = |O\,O_C|$, and the distance l corresponding to different types of mirrors is shown in Table 1.

If the intrinsic matrix of the virtual camera is:

$$\mathbf{K}_C = \begin{bmatrix} f_x & s & u_0 \\ 0 & f_y & v_0 \\ 0 & 0 & 1 \end{bmatrix}, \tag{4}$$

then from (1) and (2), we have,

$$\mu\mathbf{m}_C = \mathbf{P}_C\mathbf{M}_C, \tag{5}$$

and

$$\mathbf{P}_C = \mathbf{K}_C[\mathbf{I}|\mathbf{0}], \tag{6}$$

Table 1 Distance l corresponding to different types of mirrors

Ellipsoidal	Paraboloidal	Hyperboloidal	Planar
$0 < l < 1$	$l = 1$	$0 < l < 1$	$l = 0$

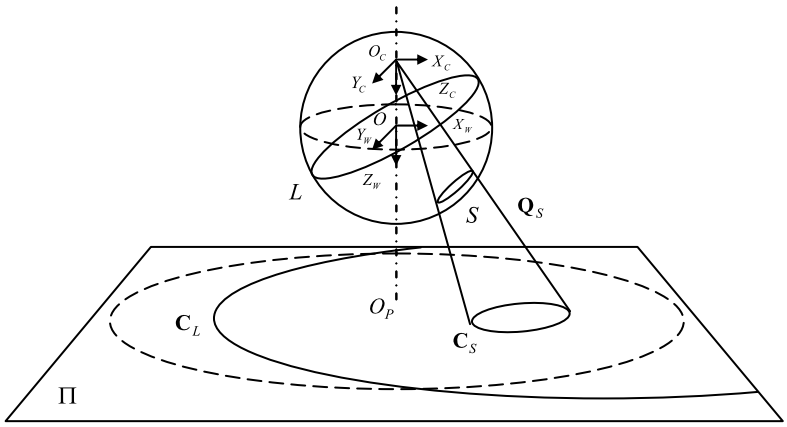

Fig. 1 A line image $\mathbf{C}_L$ and a sphere image $\mathbf{C}_S$ under the central catadioptric imaging model

where $\mathbf{M}_C$ is a point on the viewing sphere represented in the virtual camera coordinate system, and $\mathbf{m}_C$ is an image point represented in the catadioptric image coordinate system.

2.3 Equations of Line Images and Sphere Images

For a space sphere viewed by a central catadioptric camera, it is projected into a small circle S on the viewing sphere in the first step (see Fig. 1). The equation of the plane containing the small circle S in the world coordinate system (its origin is located in the center of the viewing sphere O) is:

$$n_x X_W + n_y Y_W + n_z Z_W + d_0 = 0, \tag{7}$$

where $(n_x\ n_y\ n_z)^T$ is the unit normal vector and $|d_0|$ is the distance from the origin O to the plane. Similarly, the image of a space line on the viewing sphere is a great circle L (see Fig. 1), which lies on a plane $(n_x\ n_y\ n_z\ 0)^T$ passing through the origin O. Obviously, a great circle can be considered as a special case of a small circle when the distance from the origin to the plane is zero. Therefore, there exists a unified framework to represent the projections of a line and a sphere on the viewing sphere. Consequently, the equations for a sphere derived from (7) can be changed into the equations for a line by setting $d_0 = 0$.

The projection center O_C and the small circle S form a cone (it may be not a right cone) and the equation for the cone in the virtual camera coordinate system is:

$$\mathbf{Q}_S = \begin{bmatrix} (l^2-1)n_x^2 + (d_0 - l\cdot n_z)^2 & (l^2-1)n_x n_y & (ld_0 - n_z)n_x & 0 \\ (l^2-1)n_x n_y & (l^2-1)n_y^2 + (d_0 - l\cdot n_z)^2 & (ld_0 - n_z)n_y & 0 \\ (ld_0 - n_z)n_x & (ld_0 - n_z)n_y & (d_0^2 - n_z^2) & 0 \\ 0 & 0 & 0 & 0 \end{bmatrix}. \tag{8}$$

Then a point $\mathbf{M}_C = [X_C\ Y_C\ Z_C\ 1]^T$ on the cone $\mathbf{Q}_S$ in the virtual camera coordinate system satisfies:

$$\mathbf{M}_C^T \mathbf{Q}_S \mathbf{M}_C = 0, \tag{9}$$

or

$$\bar{\mathbf{M}}_C^T \bar{\mathbf{Q}}_S \bar{\mathbf{M}}_C = 0, \tag{10}$$

where $\bar{\mathbf{M}}_C = [X_C\ Y_C\ Z_C]^T$ are the inhomogeneous coordinates of $\mathbf{M}_C$, and

$$\bar{\mathbf{Q}}_S = \begin{bmatrix} (l^2-1)n_x^2 + (d_0 - l\cdot n_z)^2 & (l^2-1)n_x n_y & (ld_0 - n_z)n_x \\ (l^2-1)n_x n_y & (l^2-1)n_y^2 + (d_0 - l\cdot n_z)^2 & (ld_0 - n_z)n_y \\ (ld_0 - n_z)n_x & (ld_0 - n_z)n_y & (d_0^2 - n_z^2) \end{bmatrix}. \tag{11}$$

From (5), the catadioptric image point of $\mathbf{M}_C$ satisfies:

$$\mu \mathbf{m}_C = \mathbf{P}_C \mathbf{M}_C = \mathbf{K}_C [\mathbf{I}|\mathbf{0}] \mathbf{M}_C = \mathbf{K}_C \bar{\mathbf{M}}_C. \tag{12}$$

Since $\mathbf{K}_C$ is invertible, we obtain,

$$\bar{\mathbf{M}}_C = \mu \mathbf{K}_C^{-1} \mathbf{m}_C. \tag{13}$$

Substituting (13) into (10), we have,

$$\mathbf{m}_C^T \mathbf{K}_C^{-T} \bar{\mathbf{Q}}_C \mathbf{K}_C^{-1} \mathbf{m}_C = 0, \tag{14}$$

or

$$\lambda \mathbf{C}_S = \mathbf{K}_C^{-T} \bar{\mathbf{Q}}_S \mathbf{K}_C^{-1}, \tag{15}$$

where λ is an unknown scale factor. $\mathbf{C}_S$ is the sphere image.

By setting $d_0 = 0$ in (15), we obtain the quadratic form for a line image:

$$\lambda \mathbf{C}_L = \mathbf{K}_C^{-T} \bar{\mathbf{Q}}_L \mathbf{K}_C^{-1}, \tag{16}$$

where

$$\bar{\mathbf{Q}}_L = \begin{bmatrix} (l^2-1)n_x^2 + l^2 n_z^2 & (l^2-1)n_x n_y & -n_z n_x \\ (l^2-1)n_x n_y & (l^2-1)n_y^2 + l^2 n_z^2 & -n_z n_y \\ -n_z n_x & -n_z n_y & -n_z^2 \end{bmatrix}. \tag{17}$$

Since a line image can be seen as a special case of a sphere image (i.e., $d_0 = 0$), in the rest paper, we use $\mathbf{C}$ to denote both line images and sphere images.

3 Identical Algebraic and Geometric Properties of a Line Image or a Sphere Image

3.1 The IAC and the DIAC

The absolute conic $\boldsymbol{\Omega}_\infty$ is a conic with purely imaginary points on the plane at infinity $\boldsymbol{\pi}_\infty = [0\ 0\ 0\ 1]^T$, and its matrix form is (Hartley and Zisserman 2000, p. 63):

$$\boldsymbol{\Omega}_\infty = \begin{bmatrix} 1 & 0 & 0 \\ 0 & 1 & 0 \\ 0 & 0 & 1 \end{bmatrix}. \tag{18}$$

The mapping between $\boldsymbol{\pi}_\infty$ and its perspective image under the virtual camera is given by the planar homography $\mathbf{H} = \mathbf{K}_C \mathbf{R}$. Since the absolute conic $\boldsymbol{\Omega}_\infty$ is on $\boldsymbol{\pi}_\infty$, one may compute the image of the absolute conic (IAC) under $\mathbf{H}$ as:

$$\boldsymbol{\omega}_C = \mathbf{H}^{-T} \boldsymbol{\Omega}_\infty \mathbf{H}^{-1} = (\mathbf{K}_C \mathbf{R})^{-T} \mathbf{I} (\mathbf{K}_C \mathbf{R})^{-1} = \mathbf{K}_C^{-T} \mathbf{K}_C^{-1}. \tag{19}$$

We may define the dual image of the absolute conic (DIAC) as:

$$\boldsymbol{\omega}_C^* = \mathbf{K}_C \mathbf{K}_C^T. \tag{20}$$

3.2 The MIAC and the DMIAC

In this section, we assume $0 \le l < 1$, and discussions on $l = 1$ corresponding to a paracatadioptric camera will be given in Sect. 4.4.

Definition 1 An intrinsic matrix defined as

$$\tilde{\mathbf{K}}_C = \begin{bmatrix} f_x/\sqrt{1-l^2} & s/\sqrt{1-l^2} & u_0 \\ 0 & f_y/\sqrt{1-l^2} & v_0 \\ 0 & 0 & 1 \end{bmatrix}, \tag{21}$$

is called a modified intrinsic matrix.

Obviously, from (4) and (21) we know $\tilde{\mathbf{K}}_C$ and $\mathbf{K}_C$ satisfy,

$$\tilde{\mathbf{K}}_C = \mathbf{K}_C \begin{bmatrix} 1/\sqrt{1-l^2} & 0 & 0 \\ 0 & 1/\sqrt{1-l^2} & 0 \\ 0 & 0 & 1 \end{bmatrix}. \tag{22}$$

The modified image of the absolute conic (MIAC) satisfies,

$$\tilde{\boldsymbol{\omega}}_C = \tilde{\boldsymbol{H}}^{-T} \boldsymbol{\Omega}_\infty \tilde{\boldsymbol{H}}^{-1} = (\tilde{\mathbf{K}}_C \mathbf{R})^{-T} \boldsymbol{\Omega}_\infty (\tilde{\mathbf{K}}_C \mathbf{R})^{-1} = \tilde{\mathbf{K}}_C^{-T} \tilde{\mathbf{K}}_C^{-1}. \tag{23}$$

We may define the dual of the modified image of the absolute conic (DMIAC) as:

$$\tilde{\boldsymbol{\omega}}_C^* = \tilde{\mathbf{K}}_C \tilde{\mathbf{K}}_C^T. \tag{24}$$

3.3 Algebraic Properties Related to the MIAC

Expanding the right side of (15) using (some supplemental derivations are shown in Appendix 1)

$$\bar{\boldsymbol{Q}}_S = \frac{(d_0 - l \cdot n_z)^2}{(1-l^2)} \begin{bmatrix} 1-l^2 & 0 & 0 \\ 0 & 1-l^2 & 0 \\ 0 & 0 & 1 \end{bmatrix} - \begin{bmatrix} (1-l^2)n_x^2 & (1-l^2)n_x n_y & -(l d_0 - n_z)n_x \\ (1-l^2)n_x n_y & (1-l^2)n_y^2 & -(l d_0 - n_z)n_y \\ -(l d_0 - n_z)n_x & -(l d_0 - n_z)n_y & (l d_0 - n_z)^2/(1-l^2) \end{bmatrix}, \tag{25}$$

we obtain,

$$\lambda \mathbf{C} = \tilde{\boldsymbol{\omega}}_C - \mathbf{v}\mathbf{v}^T, \tag{26}$$

where $\tilde{\boldsymbol{\omega}}_C$ is the MIAC, and

$$\mathbf{v} = \frac{1-l^2}{d_0 - l \cdot n_z} \tilde{\mathbf{K}}_C^{-T} \begin{bmatrix} n_x \\ n_y \\ -(l \cdot d_0 - n_z)/(1-l^2) \end{bmatrix}. \tag{27}$$

3.4 Algebraic Properties Related to the DMIAC

Inverse both side of (15), and use (some supplemental derivations are shown in Appendix 2)

$$\begin{aligned} \bar{\boldsymbol{Q}}_S^{-1} &= \begin{bmatrix} n_x^2 - 1 + d_0^2 & n_x n_y & (l \cdot d_0 - n_z) n_x \\ n_x n_y & n_y^2 - 1 + d_0^2 & (l \cdot d_0 - n_z) n_y \\ (l \cdot d_0 - n_z) n_x & (l \cdot d_0 - n_z) n_y & (1-l^2)(-1+d_0^2) + (l \cdot d_0 - n_z)^2 \end{bmatrix} \\ &= (-1+d_0^2) \begin{bmatrix} 1 & 0 & 0 \\ 0 & 1 & 0 \\ 0 & 0 & (1-l^2) \end{bmatrix} + \begin{bmatrix} n_x^2 & n_x n_y & (l \cdot d_0 - n_z) n_x \\ n_x n_y & n_y^2 & (l \cdot d_0 - n_z) n_y \\ (l \cdot d_0 - n_z) n_x & (l \cdot d_0 - n_z) n_y & (l \cdot d_0 - n_z)^2 \end{bmatrix} \end{aligned} \tag{28}$$

after some manipulations, we obtain,

$$\lambda' \mathbf{C}^* = \tilde{\boldsymbol{\omega}}_C^* - \mathbf{v}'\mathbf{v}'^T, \tag{29}$$

where λ' is an unknown scale factor, and $\mathbf{C}^*$ is the inversion of the conic $\mathbf{C}$, i.e., the dual conic. $\tilde{\boldsymbol{\omega}}_C^*$ is the DMIAC, and

$$\mathbf{v}' = \frac{1}{\sqrt{(1-d_0^2)(1-l^2)}} \tilde{\mathbf{K}}_C \begin{bmatrix} n_x \\ n_y \\ l \cdot d_0 - n_z \end{bmatrix}. \tag{30}$$

From (26) and (29), it is not difficult to find that the two equations have the same mathematical form, no matter whether adopted the dual representation or not. In the rest of paper, we only discuss the geometric interpretation for $\tilde{\boldsymbol{\omega}}_C$ and determining $\tilde{\boldsymbol{\omega}}_C$ using the double-contact theorem, since $\tilde{\boldsymbol{\omega}}_C^*$ may be interpreted and determined in the same way.

3.5 Geometric Properties Related to the MIAC

Equation (26) can be rearranged as:

$$\lambda \mathbf{C} - \tilde{\boldsymbol{\omega}}_C = -\mathbf{v}\mathbf{v}^T. \tag{31}$$

Since the rank of the matrix $-\mathbf{v}\mathbf{v}^T$ is one, the rank of the matrix $\lambda \mathbf{C} - \tilde{\boldsymbol{\omega}}_C$ is one too. Consider the pencil of two conics $\mathbf{S_1}$ and $\mathbf{S_2}$, $\mathbf{S_1} + \mu \mathbf{S_2}$ represents a conic which passes through all the common points of $\mathbf{S_1}$ and $\mathbf{S_2}$ (Semple and Kneebone 1952, p. 156). Since two coincident lines (i.e., a repeated line) can be seen as a degenerate conic with rank 1, from the properties of a pencil of two conics described in (Semple and Kneebone 1952, pp. 158–161), we know that $\mathbf{C}$ is tangent to $\tilde{\boldsymbol{\omega}}_C$ at two image points, i.e., two double-contact points, and the chord of contact passing through the two tangent points satisfies (see Fig. 2):

$$\mathbf{l}_D \propto \mathbf{v}, \tag{32}$$

where $\propto$ indicates equality up to a non-zero scale factor. Note that (32) is derived from (31). Similar results can be obtained for $\mathbf{C}^*$ and $\tilde{\boldsymbol{\omega}}_C^*$.

From the discussion above, we obtain:

Proposition 1 *Each line image or each sphere image is tangent to the modified image of the absolute conic (MIAC) at two double-contact image points.*

Proposition 2 *Each dual of line image or each dual of sphere image is tangent to the dual of the modified image of the absolute conic (DMIAC) at two double-contact image points.*

3.6 Geometric Relation between the IAC and the MIAC

From (19), (23) and (22), we know the algebraic relation between the IAC $\boldsymbol{\omega}_C$ and the MIAC $\tilde{\boldsymbol{\omega}}_C$. Now we discuss on the geometric relation between the IAC and the MIAC.

Proposition 3 *The IAC and the MIAC are concentric, and centered at the principal point in the central catadioptric image.*

Proof The center of a conic is defined as the pole of the line at infinity $\mathbf{l}_\infty = (0, 0, 1)^T$ with respect to the conic. Let O' denote the center of the IAC $\boldsymbol{\omega}_C$, since $\mathbf{l}_\infty$ and O' satisfy the pole-polar relation with respect to $\boldsymbol{\omega}_C$, then we have,

$$\mathbf{l}_\infty \propto \boldsymbol{\omega}_C O'. \tag{33}$$

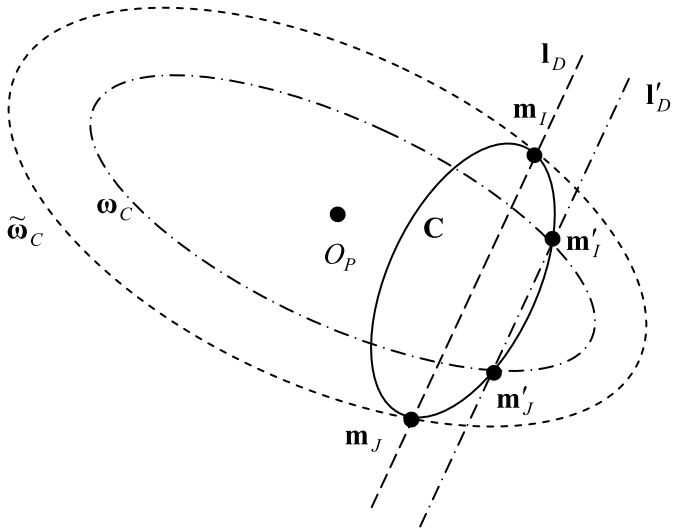

Fig. 2 Geometric relations among the MIAC $\tilde{\boldsymbol{\omega}}_C$, the IAC $\boldsymbol{\omega}_C$, and a line image or a sphere image $\mathbf{C}$

Since $\boldsymbol{\omega}_C$ is invertible and using (24), we have

$$O' \propto \boldsymbol{\omega}_C^{-1}\mathbf{l}_\infty \propto \boldsymbol{\omega}_C^{*}\mathbf{l}_\infty \propto \mathbf{K}_C\mathbf{K}_C^{T}\mathbf{l}_\infty \propto (u_0, v_0, 1)^T \propto O_P. \tag{34}$$

Therefore, the center of the IAC $\boldsymbol{\omega}_C$ is the principal point O_P. Similarly, we may obtain that O_P is also the center of the MIAC $\tilde{\boldsymbol{\omega}}_C$. □

The geometric relations between the IAC $\boldsymbol{\omega}_C$ and the MIAC $\tilde{\boldsymbol{\omega}}_C$ are illustrated in Fig. 2. From Fig. 2, we know that for a line image or a sphere image $\mathbf{C}$, it is double-contact with the MIAC. These properties are analogy of those in pinhole that the IAC is double-contact with each sphere image (Ying and Zha 2005, 2006). However, the IAC in the central catadioptric image plane has four intersection points (real and imaginary) with a line image or a sphere image $\mathbf{C}$. One of the common chords of the IAC and $\mathbf{C}$, $\mathbf{l}'_D$, shown in Fig. 2, is the polar of the projection of the center of a circle (the circle may be a great circle or a small circle corresponding the line image or the sphere image on the viewing sphere as shown in Fig. 1) with respect to $\mathbf{C}$. The common chord of the MIAC and $\mathbf{C}$, $\mathbf{l}_D$, shown in Fig. 2, is usually different from $\mathbf{l}'_D$, therefore, the pole of the $\mathbf{l}_D$ with respect to $\mathbf{C}$ is usually not the projection of the center of the circle. In case of $l = 0$, i.e., the pinhole camera, from (19), (22) and (23), we know that here the IAC and the MIAC are coincide, so are $\mathbf{l}_D$ and $\mathbf{l}'_D$. From discussions above, we know that the double contact properties with the IAC is not verified for central catadioptric systems mainly because of the re-projection from the viewing sphere to the image plane. The image of a sphere (cone) in the first step cut the viewing sphere in a planar circle that is then re-projected from a novel projection center. It shows that the matrix of equation (22) (that seems a change in focal length) "re-establishes" the double contact properties.

4 Identical Algebraic and Geometric Properties for Three Line Images or Three Sphere Images Using the Double-Contact Theorem

4.1 Geometric Properties from the Double-Contact Theorem

From discussions in Sect. 3.5, we know that three line images or three sphere images $\mathbf{C}_1, \mathbf{C}_2$ and $\mathbf{C}_3$ are all double-contact with the MIAC $\tilde{\boldsymbol{\omega}}_C$ as shown in Fig. 3. The chords of contact for $\mathbf{C}_1, \mathbf{C}_2$ and $\mathbf{C}_3$ are denoted as $\mathbf{l}_{D1}, \mathbf{l}_{D2}$ and $\mathbf{l}_{D3}$, respectively. L_1 and M_1 are a pair of opposite common chords of $\mathbf{C}_2$ and $\mathbf{C}_3$, L_2 and M_2 are a pair of opposite common chords of $\mathbf{C}_1$ and $\mathbf{C}_3$, L_3 and M_3 are a pair of opposite common chords of $\mathbf{C}_1$ and $\mathbf{C}_2$. Now, we first introduce the double-contact theorem and the converse of the double-contact theorem proposed by Evelyn et al. (1974), then derive some algebraic and geometric properties of three line images and three sphere images from these theorems.

The double-contact theorem *If* $\mathbf{C}_1$, $\mathbf{C}_2$ *and* $\mathbf{C}_3$ *are three conics having the property that there is a point* X (*not on any of the conics*) *lying on a common chord of each pair of the three conics* (*the chords in question being distinct*), *then there exists a conic* $\tilde{\boldsymbol{\omega}}_C$ *which has double contact with each of* $\mathbf{C}_1$, $\mathbf{C}_2$ *and* $\mathbf{C}_3$ (Evelyn et al. 1974, *p*. 18).

Note "a point X (not on any of the conics) lying on a common chord of each pair of the three conics" means that the three common chords (L_1, L_2 and L_3 shown as solid lines in Fig. 3) where X lies are concurrent.

Proof Since L_1, L_2 and L_3 be concurrent as shown in Fig. 3, and they may be some homogeneous vectors, it is not

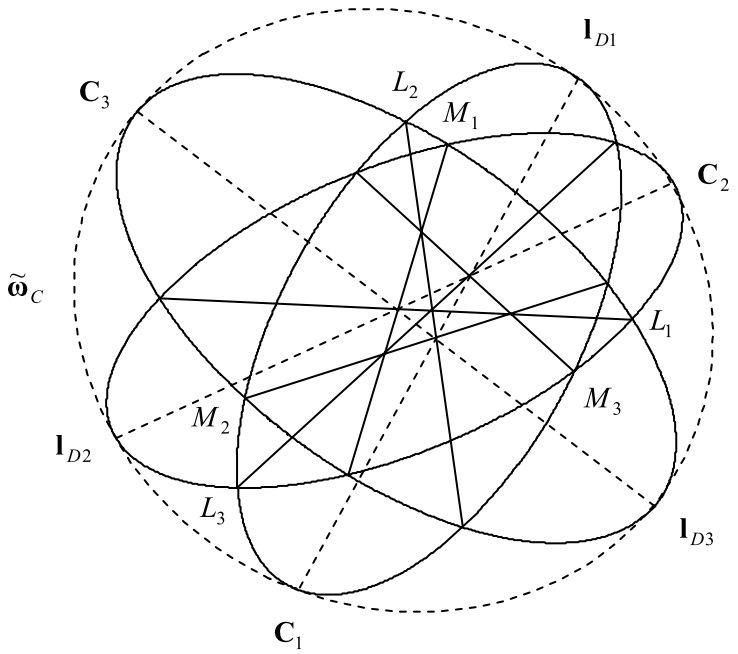

Fig. 3 Geometry for three line images or three sphere images $\mathbf{C}_1, \mathbf{C}_2, \mathbf{C}_3$ (shown in *solid lines*), and the MIAC $\tilde{\boldsymbol{\omega}}_C$ (shown in *dashed lines*). $\mathbf{C}_1, \mathbf{C}_2$ and $\mathbf{C}_3$ are all double-contact with $\tilde{\boldsymbol{\omega}}_C$.$\mathbf{l}_{D1}, \mathbf{l}_{D2}$ and $\mathbf{l}_{D3}$ (shown in *dashed lines*) are the chords of contact for $\mathbf{C}_1, \mathbf{C}_2$ and $\mathbf{C}_3$, respectively. L_1, M_1 are a pair of opposite common chords of $\mathbf{C}_2$ and $\mathbf{C}_3$, L_2, M_2 are a pair of opposite common chords of $\mathbf{C}_1$ and $\mathbf{C}_3$, L_3, M_3 are a pair of opposite common chords of $\mathbf{C}_1$ and $\mathbf{C}_2$. These six chords are shown in *solid lines*, and they form a complete quadrangle, which can be obtained using the double-contact theorem and the converse of the double-contact theorem. Note that L_1, L_2 and L_3 are concurrent

difficult to choose the scale factors of these homogeneous vectors and make them satisfy,

$$L_1 + L_2 + L_3 \equiv 0. \tag{35}$$

Note that now these scale factors are fixed, and absorbed by these vectors, i.e., they are not shown here. Since L_1 and M_1 are a pair of opposite common chords of $\mathbf{C}_2$ and $\mathbf{C}_3$, we have,

$$\mathbf{C}_2 - \mathbf{C}_3 \equiv L_1 M_1. \tag{36}$$

Note that we also choose the scale factors of $M_1, \mathbf{C}_2$ and $\mathbf{C}_3$ to make (36) identical, and no scale factor are shown here.

Similarly, for $\mathbf{C}_3$ and $\mathbf{C}_1$, we have,

$$\mathbf{C}_3 - \mathbf{C}_1 \equiv L_2 M_2. \tag{37}$$

Similarly, for $\mathbf{C}_1$ and $\mathbf{C}_2$, we have,

$$\mathbf{C}_1 - \mathbf{C}_2 \equiv L_3 M_3. \tag{38}$$

If we eliminate $\mathbf{C}_3$ between the identities (36) and (37), we obtain,

$$\mathbf{C}_1 - \mathbf{C}_2 \equiv -L_1 M_1 - L_2 M_2. \tag{39}$$

Now from (38) and (39), we obtain the identity,

$$L_1 M_1 + L_2 M_2 + L_3 M_3 \equiv 0. \tag{40}$$

If we use (35) to eliminate L_3 in (40), this reduces to

$$L_2(M_2 - M_3) \equiv L_1(M_3 - M_1). \tag{41}$$

Since L_1, L_2 are distinct (non-proportional) linear expressions, the last identity (41) shows that there must exist a constant k such that,

$$M_2 - M_3 \equiv k L_1, \tag{42}$$

and

$$M_3 - M_1 \equiv k L_2. \tag{43}$$

Similarly, these imply a third similar relation,

$$M_1 - M_2 \equiv k L_3. \tag{44}$$

At this point, we may notice that (42) demonstrates the concurrence of L_1, M_2 and M_3, and (43) and (44) have similar interpretations (see Fig. 3 for details).

Now we notice the identity

$$\begin{aligned} &4k\mathbf{C}_1 + (M_2 + M_3 - M_1)^2 \\ &\quad \equiv 4k\mathbf{C}_2 + (M_3 + M_1 - M_2)^2 \\ &\quad \equiv 4k\mathbf{C}_3 + (M_1 + M_2 - M_3)^2, \end{aligned} \tag{45}$$

where the notation, the square of a 3-vector $\mathbf{x}$, means $\mathbf{x}^2 = \mathbf{x}\mathbf{x}^T$. The equality of the first two terms, for example is equivalent to

$$\begin{aligned} 4k(\mathbf{C}_1 - \mathbf{C}_2) &\equiv (M_3 + M_1 - M_2)^2 - (M_2 + M_3 - M_1)^2 \\ &\equiv 4M_3(M_1 - M_2), \end{aligned} \tag{46}$$

which is a simple consequence of (38) and (44); and the second equality is similarly proved. If, therefore, we use $\tilde{\boldsymbol{\omega}}_C$ to

denote any one of the three identical expressions (46), we will find that the conic $\tilde{\boldsymbol{\omega}}_C$ has double contact with each of $\mathbf{C}_1, \mathbf{C}_2$ and $\mathbf{C}_3$. The reasons are as follows: By comparing (46) with (26), we may obtain that the chords of contact satisfy:

$$\mathbf{l}_{D1} \propto M_2 + M_3 - M_1, \tag{47}$$

$$\mathbf{l}_{D2} \propto M_3 + M_1 - M_2, \tag{48}$$

$$\mathbf{l}_{D3} \propto M_1 + M_2 - M_3, \tag{49}$$

corresponding to $\mathbf{C}_1, \mathbf{C}_2$ and $\mathbf{C}_3$, respectively. Therefore, we have,

$$\begin{aligned}\tilde{\boldsymbol{\omega}}_C &\propto 4k\mathbf{C}_1 + (M_2 + M_3 - M_1)^2 \\ &\equiv 4k\mathbf{C}_2 + (M_3 + M_1 - M_2)^2 \\ &\equiv 4k\mathbf{C}_3 + (M_1 + M_2 - M_3)^2,\end{aligned} \tag{50}$$

where the notation, the square of a 3-vector $\mathbf{x}$, means $\mathbf{x}^2 = \mathbf{x}\mathbf{x}^T$, and k is a scale factor which can be determined from L_1, L_2, L_3, M_1, M_2 and M_3. Note that though L_i and M_i, $(i = 1, 2, 3)$ may be some homogeneous vectors, here we choose the scale factors of these homogeneous vectors to satisfy $L_1 + L_2 + L_3 \equiv 0$, and $L_1M_1 + L_2M_2 + L_3M_3 \equiv 0$ (see Evelyn et al. 1974, for details). □

Furthermore, we find that each chord of contact (shown as dashed lines in Fig. 3) passes through two intersection points between the opposite sides of the complete quadrangle. This gives a geometric construction method to determine the chords of contact $\mathbf{l}_{Di}$ $(i = 1, 2, 3)$, i.e., $\mathbf{v}_i$ in (31). Note that Agrawal and Davis (2003) only gave an algebraic method to solve for $\mathbf{v}_i$ and the solution for $\mathbf{v}_i$ is a very important part in the previous calibration algorithms (Agrawal and Davis 2003; Ying and Zha, 2005, 2006), but no geometric interpretation was given in these papers.

The converse of the double-contact theorem *If three conics* $\mathbf{C}_1, \mathbf{C}_2, \mathbf{C}_3$ *all have double contact with another conic* $\tilde{\boldsymbol{\omega}}_C$, *then each two of* $\mathbf{C}_1, \mathbf{C}_2$ *and* $\mathbf{C}_3$ *have a "distinguished" pair of opposite common chords, and the three such pairs of common chords being the pairs of opposite sides of a complete quadrangle* (Evelyn et al. 1974, *p*. 19).

The proof of this theorem is omitted here. Therefore, from the converse of the double-contact theorem, we know that L_1, M_1, L_2, M_2, L_3, M_3 form a complete quadrangle (shown as solid lines in Fig. 3).

4.2 Interpretation for Sphere Images

Here we assume $0 \leq l < 1$, and discussions on $l = 1$ corresponding to a paracatadioptric camera will be given in Sect. 4.4. From Proposition 1, we know that each sphere image is tangent to the MIAC at two double-contact image points. The MIAC has only purely imaginary points, but it shares the properties of any conic, such as the double-contact theorem. Therefore, three sphere images and the MIAC may be interpreted by the double-contact theorem. An example of three sphere images is shown in the middle of Fig. 4(a). Three pairs of common chords of each two of the three sphere images are drawn in Fig. 4(b). Though the intersection points of each two of these three sphere images are all imaginary points, the common chords of each two may be real lines shown as in Fig. 4(b). The MIAC is not shown in Fig. 4 since it cannot be drawn in the real plane. Note that the concurrent point of three common chords may be not located in the principal point (see Fig. 4(a)).

4.3 Interpretation for Line Images

Here we assume $0 < l < 1$, whereas the line image under $l = 0$ corresponding to a pinhole camera is a degenerate case and discussions on $l = 1$ corresponding to a paracatadioptric camera will be given in Sect. 4.4. Since a line image is a special case of a sphere image, from the discussions in Sect. 4.2, we may easily obtain that three line images and the IMAC satisfy the double-contact theorem. Here we give another very intuitive interpretation.

From discussions in Barreto and Araujo (2001), we know, for three line images, a common chord of each pair of the three line images $\mathbf{C}_1, \mathbf{C}_2$ and $\mathbf{C}_3$, should pass through the principal point O_P (See Fig. 5). It is not difficult to find that these satisfy the condition of the double-contact theorem. This interpretation is very intuitive. Note that the other opposite common chords have no real intersection points with the three line images and are not shown in Fig. 5. Another important fact should be emphasized is that from the three common chords passing through the principal point, we may only obtain that, for these three line images, there exist a conic which has double contact with each of three line images, but, we cannot obtain that the conic is invariant when the three line images are changed. From Proposition 1, we can obtain that the conic is invariant, which is the IMAC.

4.4 Interpretation for Paracatadioptric Camera

As we know, line images and sphere images are both circles under paracatadioptric cameras, i.e., $l = 1$, if the skew is zero and the aspect ratio is unitary. Similar to line images under $0 < l < 1$ in Sect. 4.3, for three paracatadioptric line images, a common chord of each pair of the three line images $\mathbf{C}_1, \mathbf{C}_2$ and $\mathbf{C}_3$, should pass through the principal point O_P (See Fig. 6).

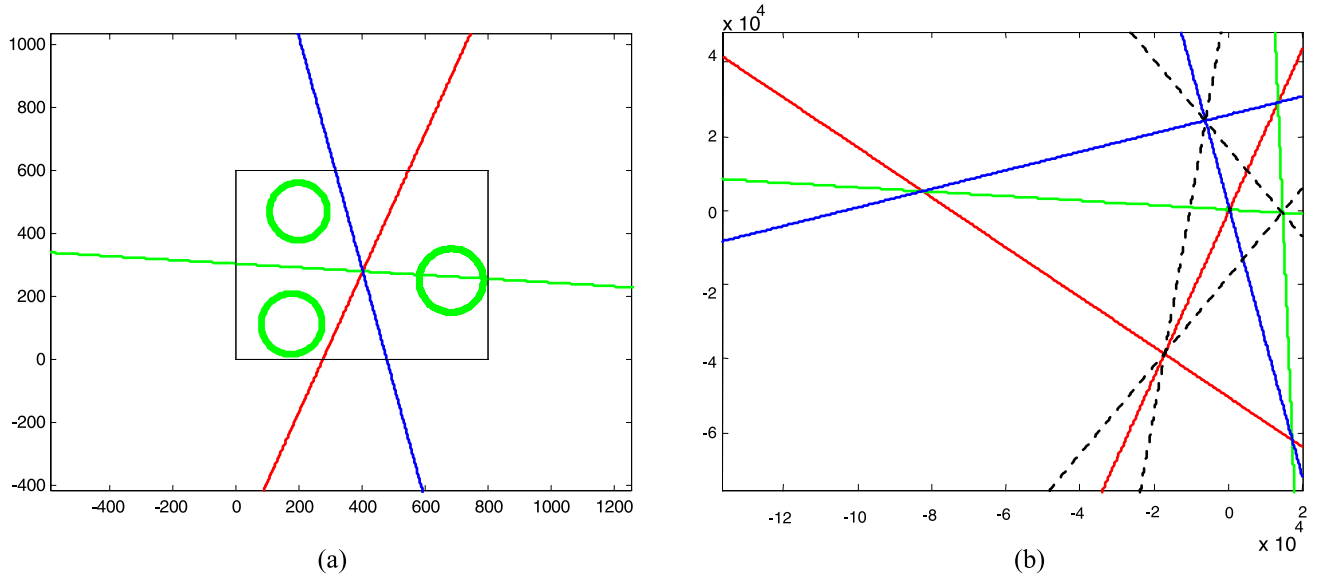

Fig. 4 A simulated image 800 × 600 containing three sphere images is shown in the middle of (**a**). Though the intersection points of each two of these three sphere images are all imaginary points, the common chords of each two may be real lines. Note that only three common chords are visible in (**a**). (**b**) Obtained by zooming out on (**a**). Now three pairs of opposite common chords of each two of these three sphere images are visible as shown in *solid lines*. We may find that these six chords form a complete quadrangle. The three chords of contact are shown as *dashed lines*

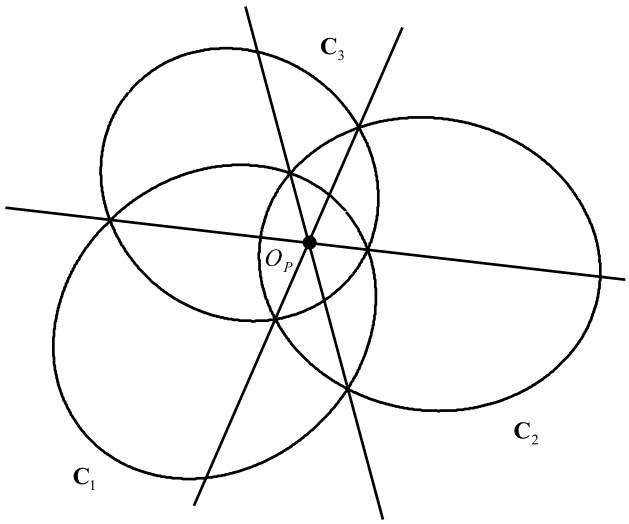

Fig. 5 Three line images from a central catadioptric camera with a hyperbolic/elliptical mirror

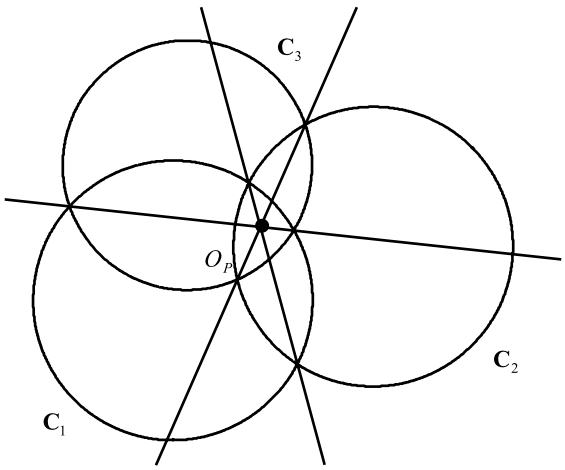

Fig. 6 Three line images under a central paracatadioptric camera

The three-conics theorem *If three conics pass through two given points, then the lines joining the other two intersections of each pair of the conics are concurrent* (Evelyn et al. 1974, *p.* 11).

If the two given points are taken to be the circular points at infinity, we obtain the familiar theorem that the radical axes of three circles, taken by pairs, are concurrent (Evelyn et al. 1974, p. 15). The concurrent point is called the radical center. Note that for line images, the radical center is located in the principal point, but for sphere images, the radical center may be not (see Fig. 7).

Obviously, three paracatadioptric line or sphere images satisfy the double-contact theorem. However, it should be noted that, here the conic which each line image and each sphere image is double-contact with is degenerated (as an envelope) into a point-pair (Evelyn et al. 1974, p. 22; Hartley and Zisserman 2000, p. 32), i.e., the circular points. That means all paracatadioptric line and sphere images pass through two invariant points (a degenerate conic), the circular points in the image plane.

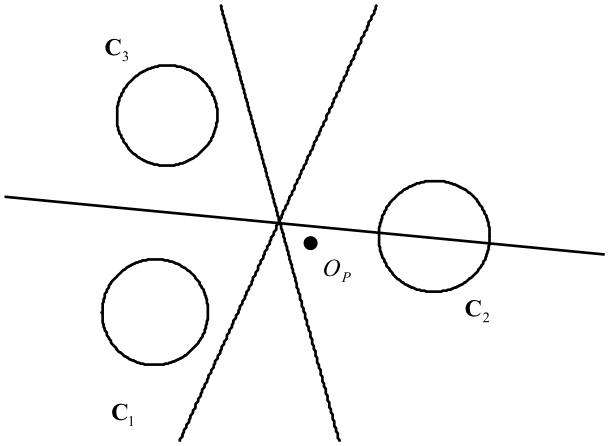

Fig. 7 Three sphere images under a central paracatadioptric camera

5 Calibration

5.1 A Counting Argument

Since it requires knowing some results presented in Ying and Hu (2004), one may skip this section if not very familiar with that paper. For the convenience of discussions, the camera intrinsic matrix $\mathbf{K}_C$ defined in (4) is rewritten and decomposed into the product of two matrices:

$$\mathbf{K}_C = \begin{bmatrix} f_x & s & u_0 \\ 0 & f_y & v_0 \\ 0 & 0 & 1 \end{bmatrix} = \begin{bmatrix} r \cdot f_e & s & u_0 \\ 0 & f_e & v_0 \\ 0 & 0 & 1 \end{bmatrix} = \begin{bmatrix} r & s' & u_0 \\ 0 & 1 & v_0 \\ 0 & 0 & 1 \end{bmatrix} \cdot \begin{bmatrix} f_e & 0 & 0 \\ 0 & f_e & 0 \\ 0 & 0 & 1 \end{bmatrix}. \tag{51}$$

Now we discuss how many constrains on the intrinsic parameters r, s', u_0, v_0, f_e and the distance l (defined in Sect. 2.2) may be provided by three sphere images (discussions on three line images will be given later). For one sphere image, it provides two invariants (Ying and Hu 2004):

$$d(bd - ae) - e(be - cd) = 0, \tag{52}$$

$$b(bd - ae) f_e^2 - e(bf - de)(l^2 - 1) = 0, \tag{53}$$

where a, b, c, d, e, f are the coefficients in the metric projection of a sphere image (the definition of the metric projection can be seen in Ying and Hu 2004). Given three sphere images, we may obtain three equations on r, s', u_0 and v_0 from (52) (Ying and Hu 2004), and other two equations on r, s', u_0 and v_0 can be obtained from (53). That means only one equation on f_e and l can be provided by three sphere images. The reasons are as follows:

Equation (53) can be rewritten as:

$$\frac{f_e^2}{l^2 - 1} = \frac{e(bf - de)}{b(bd - ae)}. \tag{54}$$

Therefore, for three sphere images, eliminating $f_e^2/(l^2 - 1)$ in the three equations from (53), then two equations on r, s', u_0 and v_0 are obtained. For central catadioptric cameras, l is usually known. If l is unknown, we cannot obtain f_e and l separately only from three or more sphere images if any other information is not given.

For one line image, it provides three invariants (Ying and Hu 2004):

$$d(bd - ae) - e(be - cd) = 0, \tag{55}$$

$$bf + de(l^2 - 1) = 0, \tag{56}$$

$$d(bd - ae) f_e^2 + f(bf - de) = 0, \tag{57}$$

where a, b, c, d, e, f are the coefficients in the metric projection of a sphere image (Ying and Hu 2004). Given three line images, we may obtain three equations on r, s', u_0 and v_0 from (55) (Ying and Hu 2004), and other four more equations on r, s', u_0 and v_0 can be obtained from (56) and (57). That means one equation on f_e and one equation on l can be obtained from three line images. Therefore, we may determine f_e and l separately only from three line images.

One easy way to solve the ambiguous in three sphere images is to use the significant characteristic of an actual central catadioptric image whose boundary is usually an ellipse. After obtaining r, s', u_0 and v_0, we may transform this boundary ellipse into a circle. If the FOV is know in advance, then we have,

$$r_b(l + \cos(\varphi_{\text{FOV}}/2)) = f_e \sin(\varphi_{\text{FOV}}/2), \tag{58}$$

where φ_{FOV} is the angle of the FOV, and r_b is the radius of the boundary circle. Therefore, f_e and l can be solved with this additional equation.

5.2 Determining the MIAC with the Double-Contact Points

For each line image or each sphere image $\mathbf{C}$, its corresponding line $\mathbf{l}_D \propto \mathbf{v}$ can be determined (How to find $\mathbf{v}$ up to an unknown scale factor has been given in Agrawal and Davis (2003), i.e., $\|\mathbf{v}\|$ is yet unknown.) Therefore, the two intersection points of the obtained line $\mathbf{l}_D$ and the original conic $\mathbf{C}$, i.e., $\mathbf{m}_I$ and $\mathbf{m}_J$, can be obtained (see Fig. 2). From discussion in Sect. 3, we know that the two intersection points $\mathbf{m}_I$ and $\mathbf{m}_J$ also lie on the MIAC $\tilde{\boldsymbol{\omega}}_C$. Therefore, six points on $\tilde{\boldsymbol{\omega}}_C$ can be obtained from three line images or three sphere images. Since five points define a conic, the six points are sufficient to estimate $\tilde{\boldsymbol{\omega}}_C$. As we know, the MIAC should be positive definite. The linear methods may fail in the case

where the computed MIAC is not positive definite. However, this did not occur in our experiments, except in the case where the noises are large. After obtaining $\tilde{\boldsymbol{\omega}}_C$, it is not difficult to determine $\mathbf{v}$, i.e., $\|\mathbf{v}\|$ from (31).

5.3 The Calibration Algorithm by Finding the Double-Contact Points

The complete calibration algorithm by finding the double-contact points consists of the following steps:

1. Fit conic curves, then obtain $\mathbf{C}_i$.
2. Find $\mathbf{l}_{Di} \propto \mathbf{v}_i$, then obtain the intersection points of $\mathbf{C}_i$ and $\mathbf{l}_{Di}$, then determine $\tilde{\boldsymbol{\omega}}_C$.
3. If $\tilde{\boldsymbol{\omega}}_C$ is not positive definite, then stop.
4. Determine $\tilde{K}_C$ by using the Cholesky factorization of $\tilde{\boldsymbol{\omega}}_C$. Then obtain $\mathbf{K}_C$ from $\tilde{\mathbf{K}}_C$ using (22).
5. Obtain $\mathbf{v}_i$, then solve for the extrinsic parameters of the camera. (See Agrawal and Davis 2003; Teramoto and Xu 2002 for details.)

5.4 Determining the MIAC Using the Double-Contact Theorem

Given three line or three sphere images $\mathbf{C}_i$ $(i = 1, 2, 3)$, from (50), we may determine the MIAC $\tilde{\boldsymbol{\omega}}_C$ as:

$$\tilde{\boldsymbol{\omega}}_C \propto 4k\mathbf{C}_1 + (M_2 + M_3 - M_1)^2 + 4k\mathbf{C}_2 + (M_3 + M_1 - M_2)^2 + 4k\mathbf{C}_3 + (M_1 + M_2 - M_3)^2. \tag{59}$$

As we know, the MIAC $\tilde{\boldsymbol{\omega}}_C$ should be positive definite. The linear methods may fail in the case where the computed MIAC $\tilde{\boldsymbol{\omega}}_C$ is not positive definite. However, this did not occur in our experiments, except in the case where the noises are large. After obtaining $\tilde{\boldsymbol{\omega}}_C$, it is not difficult to determine $\mathbf{v}_i$ from (31).

5.5 The Calibration Algorithm Using the Double-Contact Theorem

The complete calibration algorithm using the double-contact theorem consists of the following steps:

1. Fit conic curves, then obtain $\mathbf{C}_i$.
2. Determine $\tilde{\boldsymbol{\omega}}_C$ using the double-contact theorem.
3. If $\tilde{\boldsymbol{\omega}}_C$ is not positive definite, then stop.
4. Determine $\tilde{\mathbf{K}}_C$ by using the Cholesky factorization of $\tilde{\boldsymbol{\omega}}_C$. Then obtain $\mathbf{K}_C$ from $\tilde{\mathbf{K}}_C$ using (22).
5. Obtain $\mathbf{v}_i$, then solve for the extrinsic parameters of the camera. (See Agrawal and Davis 2003; Teramoto and Xu 2002 for details.)

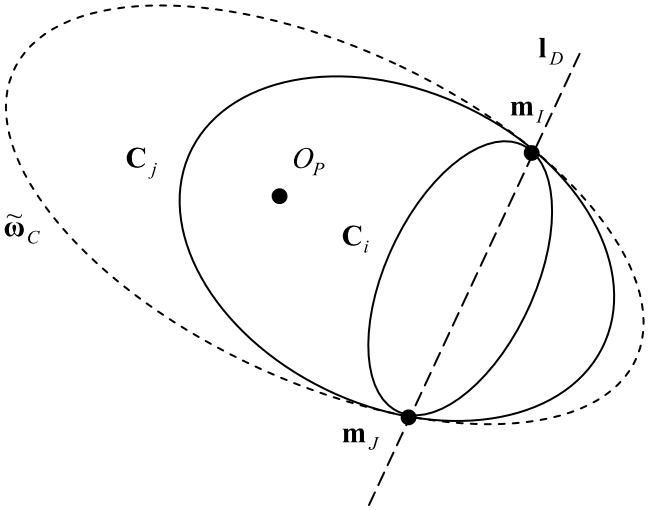

Fig. 8 Geometry for the degenerate case of the two linear calibration methods proposed in this paper

5.6 Singularities

Like almost any algorithm, these two calibration algorithms have singularities. In practice, it is important to be aware of the singularities in order to obtain reliable results by avoiding them.

As stated in Sect. 3.5, each line image and each sphere image provides two double-contact points on the MIAC. However, if two line images or two sphere images are double-contact with the MIAC at the same two points, there are only two constrains on the MIAC obtained from the two line images or two sphere images, not four in general cases. For two line images or two sphere images, $\mathbf{C}_i$ and $\mathbf{C}_j$ with the same double-contact points are shown in Fig. 8. Obviously, they should have the same chord of contact, $\mathbf{l}_D$. From (32) and (27), we know,

$$\mathbf{l}_D \propto \mathbf{v} \propto \tilde{\mathbf{K}}_C^{-T} \begin{bmatrix} n_x \\ n_y \\ -(l \cdot d_0 - n_z)/(1 - l^2) \end{bmatrix}. \tag{60}$$

Let n_x, n_y, n_z, d_0 corresponding to $\mathbf{C}_i$ and $\bar{n}_x$, $\bar{n}_y$, $\bar{n}_z$, $\bar{d}_0$ corresponding to $\mathbf{C}_j$ (note that if $\mathbf{C}_i$ and $\mathbf{C}_j$ are two line images, then $d_0 = 0$ and $\bar{d}_0 = 0$), if they satisfy,

$$\begin{bmatrix} n_x \\ n_y \\ -(l \cdot d_0 - n_z)/(1 - l^2) \end{bmatrix} \propto \begin{bmatrix} \bar{n}_x \\ \bar{n}_y \\ -(l \cdot \bar{d}_0 - \bar{n}_z)/(1 - l^2) \end{bmatrix}, \tag{61}$$

then $\mathbf{C}_i$ and $\mathbf{C}_j$ have the same chord of contact, $\mathbf{l}_D$, i.e., have the same double-contact points with the MIAC. In this degenerate case, the two common chords of the two conics are coincident, not distinct, however, the double-contact

theorem requires that the common chords must be distinct. Therefore, this case is also degenerate if the double-contact theorem is used. From discussions above, we have,

Proposition 4 *For three line images or three sphere images, if two of them satisfy* (61)*, then the two linear calibration methods proposed in this paper are both degenerate.*

6 Experiments

We perform a number of experiments, both simulated and real, to test our algorithms with respect to noise sensitivity, and make comparisons with the following algorithms:

- **DCP**: By finding the double-contact points with the MIAC.
- **DCT**: Using the double-contact theorem related to the MIAC.
- **Orth**: Using the orthogonal constraints (Zhang et al. 2007) related to the MIAC.
- **SDP**: Employing semi-definite programming (Agrawal and Davis 2003) with the representation of the MIAC.
- **GI:** Using geometric invariants with Levenberg–Marquardt algorithm.

Note that for **DCP**, **DCT**, **Orth** and **SDP**, there also exist the calibration methods with the DMIAC correspondingly. Due to the lack of space, there are not discussed here. In the real experiments, we use a perspective camera with a hyperbolic mirror, designed by the Center for Machine Perception, Czech Technical University, its field of view (FOV) is 217.2 degree, and the parameter of the hyperbolic mirror is $l = 0.966$. Here we assume that the parameter l is known in advance. Due to lack of space, we are only able to demonstrate the experimental results using sphere images, and experiments with line images are not shown here.

6.1 Calibration with Simulated Data

The simulated catadioptric camera has the following parameters: $f_x = 450$, $f_y = 450$, $s = 0$, $u_0 = 400$, $v_0 = 300$ and $l = 0.966$. The resolution of the simulated image is 800×600. We generate an image containing three sphere images uniformly distributed within the image as shown in the middle of Fig. 4(a). On each sphere image we choose 100 points. Gaussian noise with zero-mean and σ standard deviation is added to these image points. We vary the noise level σ from 0 to 2 pixels. The conic fitting algorithm presented in Fitzgibbon et al. (1999) is used here. For each noise level, we perform 1,000 independent trials, and the mean values and standard deviations of these recovered parameters are computed over each run. The estimated results of these experiments are shown in Fig. 9. Since the performances of f_x and f_y, u_0 and v_0 are both very similar, the estimated results for f_y and v_0 are not shown here. The results from **DCP** are selected as the initial values for **GI** used in Levenberg–Marquardt algorithm. In fact, there are only very small differences among the estimated results from **DCP**, **DCT**, **Orth** and **SDP**, whereas the results from **GI** are better. We compare the runtimes of these methods using MATLAB implementations of all algorithms on a 1.7 GHz Pentium IV processor. Note that real-time performance is not expected for any of the algorithms under MATLAB, and our only goal is to provide comparison. All results are averaged over 1,000 trials and recorded in Table 2. Since SDP is a convex optimization problem and has polynomial worst-case complexity, and Levenberg–Marquardt algorithm is a nonlinear least squares problem, the runtimes of **GI**, **SDP** are about ten times slower than that using **DCP**, **DCT** and **Orth**.

6.2 Calibration with Real Data

The test sphere for the real experiments is a billiard ball. The ball was placed in front of a white screen. We took images of the ball using the catadioptric camera. Three sphere images are taken for the calibration purpose. One of the three images is shown in Fig. 10. The resolution of these images is 800×600. Edges were extracted using Canny's edge detector and the ellipses were obtained using a least squares ellipse fitting algorithm (Fitzgibbon et al. 1999). In order to obtain unbiased results, these sphere images should be uniformly distributed within the image. The calibration results with real data are listed in Table 3. From Table 3, one may find that the calibration results using these methods are similar to one another.

Table 2 Runtimes (in seconds) for the seven algorithms

	DCT	**GEO**	**Orth**	**SDP**	**GI**
Runtime	0.076	0.093	0.057	1.598	0.482

Table 3 Calibration results with real data

	f_x	f_y	s	u_0	v_0
DCT	216.7	220.3	5.6	401.5	261.7
DCP	216.3	220.5	5.3	407.0	271.4
Orth	216.4	220.3	4.4	407.1	272.2
SDP	215.6	219.8	5.3	408.2	269.6
GI	216.1	220.4	4.7	408.8	270.2

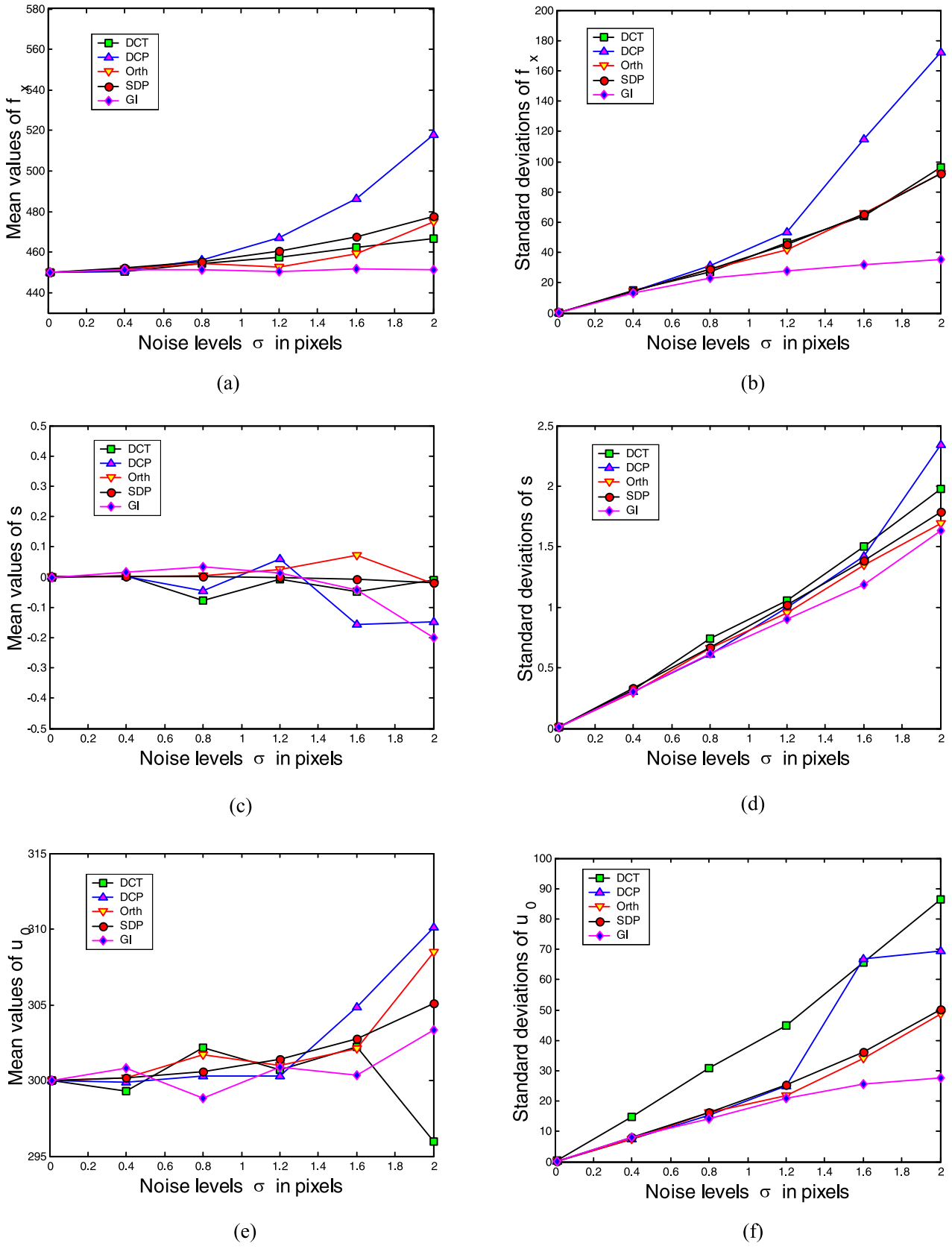

Fig. 9 The estimated results of simulated experiments. See text for details

Fig. 10 A sphere image used in the real experiments

7 Conclusions

Our main contribution is to propose the MIAC for central catadioptric cameras. By utilizing the MIAC, the identical projective geometric properties of central catadioptric line images and sphere images are discovered: Each line image and each sphere image is tangent to the MIAC at two double-contact image point. Furthermore, the double-contact theorem is employed to interpret the relation between the MIAC and line images or sphere images. These discoveries can be considered as extensions from pinhole to central catadioptric. But to prove the feasibility of these extensions is not easy and non-trivial. This is not an intuitive guess but requires rigorous proofs. In-depth analyses of the relation between the MIAC and the IAC are also presented.

These discovered properties provide new insights into the fundamental properties of line images and sphere images, especially from the aspect of their providing constraints on the camera parameters. Two new linear calibration approaches using line images or sphere images are derived from these properties. Though many linear calibration methods are proposed for central catadioptric camera using line images, there are only some nonlinear calibration approaches to sphere images. Till now, only the methods based on the MIAC may be employed for linearly calibrating catadioptric camera using sphere images and line images in a unified framework.

The relation between the MIAC and line images or sphere images under paracatadioptric cameras may be interpreted by using the special case of the double-contact theorem where the MIAC is degenerated into the circular points in the paracatadioptric image plane. We also give another very intuitive interpretation for three line images using the properties that a common chord of each pair of these three line images passing through the principal point, which satisfies the sufficient condition of the double-contact theorem. In addition, a new geometric approach is proposed to determine the chord of contact between the MIAC and a line image or a sphere image, which is a very important part in previous calibration algorithms.

Only three line images or three sphere images are required, and the intrinsic parameters are recovered linearly without making assumptions, such as, zero-skew or unitary aspect ratio. Extensive experiments on simulated and real data were performed and shown that our calibration method is an order of magnitude faster than previous nonlinear methods. A counting argument is given in details on how many constraints provided by three line images or three sphere images. Although we have studied singularities of the proposed algorithms, more thorough investigations may need to be pursued. Our future work is to explore more properties of the MIAC.

Acknowledgements The authors would like to thank the anonymous reviewers for their constructive comments which have contributed to a vast improvement of the paper. This work was supported in part by the NKBRPC 973 Grant No. 2006CB303100, the NNSFC Grant No. 60605010, and the NHTRDP 863 Grant No. 2006AA01Z302, and the Key grant Project of Chinese Ministry of Education No. 103001.

Appendix 1

We would like to give some supplemental derivations for Sect. 3.3. $\bar{\mathbf{Q}}_S$ can be decomposed as,

$$\begin{aligned}\bar{\mathbf{Q}}_S &= \begin{bmatrix} (l^2-1)n_x^2+(d_0-l\cdot n_z)^2 & (l^2-1)n_xn_y & (ld_0-n_z)n_x \\ (l^2-1)n_xn_y & (l^2-1)n_y^2+(d_0-l\cdot n_z)^2 & (ld_0-n_z)n_y \\ (ld_0-n_z)n_x & (ld_0-n_z)n_y & (d_0^2-n_z^2) \end{bmatrix} \\ &= \begin{bmatrix} (d_0-l\cdot n_z)^2 & 0 & 0 \\ 0 & (d_0-l\cdot n_z)^2 & 0 \\ 0 & 0 & \frac{(d_0-l\cdot n_z)^2}{(1-l^2)} \end{bmatrix} + \begin{bmatrix} (l^2-1)n_x^2 & (l^2-1)n_xn_y & (ld_0-n_z)n_x \\ (l^2-1)n_xn_y & (l^2-1)n_y^2 & (ld_0-n_z)n_y \\ (ld_0-n_z)n_x & (ld_0-n_z)n_y & (ld_0-n_z)^2/(l^2-1) \end{bmatrix}. \end{aligned} \tag{62}$$

Then, the first term on the right hand side of (62) is further decomposed as,

$$\begin{bmatrix} (d_0 - l\cdot n_z)^2 & 0 & 0 \\ 0 & (d_0 - l\cdot n_z)^2 & 0 \\ 0 & 0 & \frac{(d_0 - l\cdot n_z)^2}{(1-l^2)} \end{bmatrix} = \frac{(d_0 - l\cdot n_z)^2}{(1-l^2)} \begin{bmatrix} 1-l^2 & 0 & 0 \\ 0 & 1-l^2 & 0 \\ 0 & 0 & 1 \end{bmatrix} \tag{63}$$

and the last term on the right hand side of (62) is further decomposed as,

$$\begin{aligned} &\begin{bmatrix} (1-l^2)n_x^2 & (1-l^2)n_x n_y & -(ld_0 - n_z)n_x \\ (1-l^2)n_x n_y & (1-l^2)n_y^2 & -(ld_0 - n_z)n_y \\ -(ld_0 - n_z)n_x & -(ld_0 - n_z)n_y & (ld_0 - n_z)^2/(1-l^2) \end{bmatrix} \\ &= \begin{bmatrix} \sqrt{1-l^2}n_x \\ \sqrt{1-l^2}n_y \\ -(ld_0 - n_z)/\sqrt{1-l^2} \end{bmatrix} \\ &\quad \times [\,\sqrt{1-l^2}n_x \quad \sqrt{1-l^2}n_y \quad -(ld_0 - n_z)/\sqrt{1-l^2}\,] \\ &= (1-l^2) \begin{bmatrix} n_x \\ n_y \\ -(ld_0 - n_z)/(1-l^2) \end{bmatrix} \\ &\quad \times [\,n_x \quad n_y \quad -(ld_0 - n_z)/(1-l^2)\,]. \end{aligned} \tag{64}$$

Appendix 2

We would like to give some supplemental derivations for Sect. 3.4. Firstly we derive $\bar{\mathbf{Q}}_S^{-1}$ from $\bar{\mathbf{Q}}_S$ defined in (11), and then show the decomposition of $\bar{\mathbf{Q}}_S^{-1}$ in details. As we know,

$$\bar{\mathbf{Q}}_S^{-1} \propto \bar{\mathbf{Q}}_S^{*} \propto \begin{bmatrix} a_{11} & a_{12} & a_{13} \\ a_{12} & a_{22} & a_{23} \\ a_{13} & a_{23} & a_{33} \end{bmatrix}, \tag{65}$$

where $\bar{\mathbf{Q}}_S^{*}$ is the adjoint of matrix $\bar{\mathbf{Q}}_S$. Note that $\bar{\mathbf{Q}}_S^{*}$ is a symmetric matrix. Therefore, from (11), we have,

$$\begin{aligned} a_{11} &= ((l^2-1)n_y^2 + (d_0 - l\cdot n_z)^2)(d_0^2 - n_z^2) \\ &\quad - (ld_0 - n_z)n_y(ld_0 - n_z)n_y \\ &= (l\cdot n_z - d_0)^2(n_x^2 - 1 + d_0^2), \\ a_{22} &= ((l^2-1)n_y^2 + (d_0 - l\cdot n_z)^2)(d_0^2 - n_z^2) \\ &\quad - (ld_0 - n_z)n_y(ld_0 - n_z)n_y \\ &= (l\cdot n_z - d_0)^2(n_x^2 - 1 + d_0^2), \\ a_{33} &= ((l^2-1)n_y^2 + (d_0 - l\cdot n_z)^2)((l^2-1)n_y^2 \\ &\quad + (d_0 - l\cdot n_z)^2) - (l^2-1)n_x n_y (l^2-1)n_x n_y \\ &= (l\cdot n_z - d_0)^2((1-l^2)(-1 + d_0^2) + (l\cdot d_0 - n_z)^2), \\ a_{12} &= -(l^2-1)n_x n_y (d_0^2 - n_z^2) + (ld_0 - n_z)n_y(ld_0 - n_z)n_x \\ &= (l\cdot n_z - d_0)^2 n_x n_y. \\ a_{13} &= (l^2-1)n_x n_y (ld_0 - n_z)n_y \\ &\quad - ((l^2-1)n_y^2 + (d_0 - l\cdot n_z)^2)(ld_0 - n_z)n_x \\ &= (l\cdot n_z - d_0)^2(ld_0 - n_z)n_x, \\ a_{23} &= (l^2-1)n_x n_y (ld_0 - n_z)n_x \\ &\quad - ((l^2-1)n_x^2 + (d_0 - l\cdot n_z)^2)(ld_0 - n_z)n_y \\ &= (l\cdot n_z - d_0)^2(ld_0 - n_z)n_y. \end{aligned} \tag{66}$$

After eliminating $(l\cdot n_z - d_0)^2$ from a_{ij}, we may obtain (28), note that, the last term on the right hand side of (28) can be further decomposed as,

$$\begin{aligned} &\begin{bmatrix} n_x^2 & n_x n_y & (l\cdot d_0 - n_z)n_x \\ n_x n_y & n_y^2 & (l\cdot d_0 - n_z)n_y \\ (l\cdot d_0 - n_z)n_x & (l\cdot d_0 - n_z)n_y & (l\cdot d_0 - n_z)^2 \end{bmatrix} \\ &= \begin{bmatrix} n_x \\ n_y \\ l\cdot d_0 - n_z \end{bmatrix} [\,n_x \quad n_y \quad l\cdot d_0 - n_z\,]. \end{aligned} \tag{67}$$

References

Agrawal, M., & Davis, L. S. (2003). Camera calibration using spheres: a semi-definite programming approach. In *Proceedings of the IEEE international conference on computer vision* (pp. 782–791).

Aliaga, D. G. (2001). Accurate catadioptric calibration for real-time pose estimation of room-size environments. In *Proceedings of the international conference on computer vision* (pp. 127–134).

Baker, S., & Nayar, S. (1998). A theory of catadioptric image formation. In *Proceedings of IEEE international conference on computer vision* (pp. 35–42), Bombay.

Barreto, J. P., & Araujo, H. (2001). Issues on the geometry of central catadioptric imaging. In *Proceedings of the IEEE international conference on computer vision and pattern recognition*, Kauai, HI, USA.

Barreto, J. P., & Araujo, H. (2005). Geometric properties of central catadioptric line images and their application in calibration. *IEEE Transactions on Pattern Analysis and Machine Intelligence*, *27*(8), 1327–1333.

Barreto, J. P., & Araujo, H. (2006). Fitting conics to paracatadioptric projection of lines. *Computer Vision and Image Understanding*, *101*(3), 151–165.

Bogner, S. (1995). An introduction to panospheric imaging. In *Proceedings of the IEEE conference systems, man, and cybernetics* (pp. 3099–3116), Vancouver, BC.

Evelyn, C. J. A., Money-Coutts, G. B., & Tyrrell, J. A. (1974). *The seven circles theorem and other new theorems*. London: Stacey International.

Fitzgibbon, A., Pilu, M., & Fisher, R. (1999). Direct least square fitting of ellipses. *IEEE Transactions on Pattern Analysis and Machine Intelligence*, *21*(5), 476–480.

Geyer, C., & Daniilidis, K. (1999). Catadioptric camera calibration. In *Proceedings of the international conference on computer vision* (pp. 398–404), Kerkyra, Greece, 20–23 September 1999.

Geyer, C., & Daniilidis, K. (2001). Catadioptric projective geometry. *International Journal of Computer Vision*, *43*, 223–243.

Geyer, C., & Daniilidis, K. (2002). Paracatadioptric camera calibration. *IEEE Transactions on Pattern Analysis and Machine Intelligence*, *24*(5), 687–695.

Gluckman, J., & Nayar, S. K. (2001). Catadioptric stereo using planar mirrors. *International Journal of Computer Vision*, *44*(1), 65–79.

Hartley, R., & Zisserman, A. (2000). *Multiple view geometry in computer vision*. Cambridge: Cambridge University Press.

Hecht, E., & Zajac, A. (1997). *Optics* (3rd ed.). Reading: Addison–Wesley.

Hong, J., Tan, X., Weiss, R., & Riseman, E. (1991). Image-based homing. In *IEEE international conference robotics and automation* (pp. 620–625).

Kang, S. (2000). Catadioptric self-calibration. In *IEEE conference computer vision and pattern recognition* (pp. 201–207), Hilton Head Island, SC, 13–15 June 2000.

Nalwa, V. S. (1996). *A true omnidirectional viewer*. Technical Report, Bell Laboratories, Holmdel, NJ 07733, USA.

Nayar, S. K. (1988). Sphereo: Recovering depth using a single camera and two specular spheres. In *Proceedings of SPIE: optics, illumination, and image sensing for machine vision II*.

Nene, S., & Nayar, S. (1998). Stereo with mirrors. In *Proceeding international conference on computer vision* (pp. 1087–1094), Bombay, India, 3–5 January, 1998.

Semple, J., & Kneebone, G. (1952). *Algebraic projective geometry*. Oxford: Oxford Science.

Svoboda, T., Pajdla, T., & Hlavac, V. (1998). Epipolar geometry for panoramic cameras. In *Proceedings of the 5th European conference on computer vision* (pp. 218–231).

Swaminathan, R., Grossberg, M. D., & Nayar, S. (2006). Non-single viewpoint catadioptric cameras: geometry and analysis. *International Journal of Computer Vision*, *66*(3), 211–229.

Teramoto, H., & Xu, G. (2002). Camera calibration by a single image of balls: from conics to the absolute conic. In *Proceedings Asian conference computer vision* (pp. 499–506).

Yagi, Y., & Kawato, S. (1990). Panorama scene analysis with conic projection. In *Proceedings of IEEE/RSJ international workshop on intelligent robots and systems* (pp. 181–187).

Yagi, Y., & Yachida, M. (2004). Real-time omnidirectional image sensors, *International Journal of Computer Vision 58*(3), 173–207.

Ying, X., & Hu, Z. (2004). Catadioptric camera calibration using geometric invariants. *IEEE Transactions on Pattern Analysis and Machine Intelligence*, *26*(10), 1260–1271.

Ying, X., & Zha, H. (2005). Linear approaches to camera calibration from sphere images or active intrinsic calibration using vanishing points. In *Proceedings of IEEE international conference on computer vision* (pp. 596–603), China.

Ying, X., & Zha, H. (2006). Geometric interpretations of the relation between the image of the absolute conic and sphere images. *IEEE Transactions on Pattern Analysis and Machine Intelligence*, *28*(12), 2031–2036.

Zhang, H., Wong, K., & Zhang, G. (2007). Camera calibration from images of spheres. *IEEE Transactions on Pattern Analysis and Machine Intelligence*, *29*(3), 499–503.